



# In-situ grown metal-organic framework-derived carbon-coated Fe-doped cobalt oxide nanocomposite on fluorine-doped tin oxide glass for acidic oxygen evolution reaction

Duraisamy Senthil Raja, Po-Yin Cheng, Chih-Chieh Cheng, Shun-Qin Chang, Chun-Lung Huang, Shih-Yuan Lu\*

Department of Chemical Engineering, National Tsing Hua University, Hsinchu 30013, Taiwan

## ARTICLE INFO

### Keywords:

Water electrolysis  
Metal-organic framework (MOF)  
Noble metal-free catalyst  
Acidic water oxidation  
Free-standing

## ABSTRACT

Development of stable and efficient non-noble metal based electrocatalysts for oxygen evolution reaction (OER) in acidic media is of great importance for proton exchange membrane based water electrolysis, which is indispensable for green hydrogen production. Herein, iron-doped, carbon-coated  $\text{Co}_3\text{O}_4$  nanocomposite derived from a cobalt metal-organic framework, is grown in-situ on fluorine-doped tin oxide (FTO) glass ( $\text{Fe-Co}_3\text{O}_4/\text{C}/\text{FTO}$ ) as an efficient and a stable binder-free electrode for acidic OER. Fe doping enhances both catalytic efficiency and stability of carbon coated  $\text{Co}_3\text{O}_4$  toward acidic OER, through inducing small primary particle sizes and suitably modulated electronic structure of  $\text{Co}_3\text{O}_4$ , and better catalyst/substrate adhesion.  $\text{Fe-Co}_3\text{O}_4/\text{C}/\text{FTO}$  exhibits impressive electrocatalytic performances in 0.5 M  $\text{H}_2\text{SO}_4$ , with a low overpotential of 396 mV at 10  $\text{mA cm}^{-2}$  and a small Tafel slope of 68.6  $\text{mV dec}^{-1}$ . Its electrochemical performances remain stable for over 50 h at 10  $\text{mA cm}^{-2}$ , making it a promising non-noble metal based electrocatalyst for acidic OER.

## 1. Introduction

Green energy technologies are drawing rapidly increasing attention because of the upsurge in global fossil fuels consumption and associated environmental issues.[1,2] It is well-known that electrochemically splitting water into hydrogen and oxygen to store off-peak excessive renewable energies, such as those derived from wind, sun, and water, into storable and transportable hydrogen is a critical strategy for development of green energies.[3,4] The electrolytic water splitting process is composed of two half-reactions: the hydrogen evolution reaction (HER) at cathodes and the oxygen evolution reaction (OER) at anodes, both of them are critical for overall efficiencies of the water splitting. Noble metal based electrocatalysts, such as Pt/C and  $\text{IrO}_2/\text{RuO}_2$ , although exhibiting excellent catalytic efficiency for the HER and OER, respectively, are not suitable for large scale hydrogen production because of the extreme scarcity and high cost of these noble metals.[5] A wide range of Earth-abundant element based electrocatalysts for the HER under both acidic and alkaline media have been well developed, including metal alloys,[6] chalcogenides,[7] phosphides,[8] and carbides,[9,10] as well as carbon based materials.[11]

On the contrary, investigations of non-noble metal based electrocatalysts for the OER, which is regarded as the bottleneck of the overall water splitting, have mostly focused on alkaline water splitting [12,13] because of the poor stability of non-noble metal based electrocatalysts toward acidic OER.[14,15] Robust and inexpensive OER catalysts sustainable under acidic OER conditions, however, are critical for large scale applications of proton exchange membrane (PEM) water electrolysis systems. PEM water electrolyzers are regarded as a promising and competitive approach for hydrogen production, because of their lower ohmic resistances, higher gas purity, higher current densities, and simpler and more compact system design over alkaline water electrolyzers.[15,16] Furthermore, high-pressure operations of up to 350 bar can be achieved in PEM water electrolyzers, which shrink module sizes considerably over the 30 bar maximum achievable by the alkaline water electrolysis system.[16] Considering these many advantages of PEM water electrolysis, it is indispensable to develop durable and efficient non-noble metal based electrocatalysts for acidic OER.

In recent years, cobalt based materials have been found to be potential catalysts for catalyzation of the acidic OER.[17] In particular, spinel  $\text{Co}_3\text{O}_4$  has attracted much recent attention because of its low cost,

\* Corresponding author.

E-mail address: [sylu@mx.nthu.edu.tw](mailto:sylu@mx.nthu.edu.tw) (S.-Y. Lu).

<https://doi.org/10.1016/j.apcatb.2021.120899>

Received 5 August 2021; Received in revised form 30 October 2021; Accepted 2 November 2021

Available online 7 November 2021

0926-3373/© 2021 Elsevier B.V. All rights reserved.

excellent electrocatalytic properties, and high corrosion stability in alkaline solutions.[18,19] Nevertheless, the application of  $\text{Co}_3\text{O}_4$  for acidic OER is limited since spinel  $\text{Co}_3\text{O}_4$  also suffers from anodic corrosion,[20] in which the formed  $\text{CoO}_2$  at high potentials decomposes into soluble  $\text{CoO}$  accompanied by release of  $\text{O}_2$  molecules.[21] Fortunately, amorphous carbon coating, serving as a protective layer, on  $\text{Co}_3\text{O}_4$  could effectively improve its OER stability in acids.[22] The porous carbon coating can effectively block the direct contact between the catalyst and the electrolyte to delay/prevent decays of the catalyst. Furthermore, partially substituting Co in  $\text{Co}_3\text{O}_4$  with a second metal has been demonstrated to substantially enhance the electrocatalytic activity and stability of  $\text{Co}_3\text{O}_4$  in alkaline media.[23,24] For instance, Lou et al. recently reported that spinel  $\text{Co}_3\text{O}_4$  nanosheets doped with Fe exhibited enhanced catalytic efficiency and stability toward the alkaline OER.[24].

In addition, metal–organic frameworks (MOFs), with their high surface areas, hybrid features and tunable porosities, multifunctionality, and good catalytic selectivity, have drawn a great deal of research attention and are advantageous precursors for construction of nanostructured core-shell metal oxides-carbon composites.[25,26] In fact, MOFs are also convenient and advantageous precursors for fabrication of carbon coated metals, alloys, and metallic sulfides and phosphides, thus emerging as a new material platform for applications in many technologically important fields.[27,28] Over the past few years, MOF-derived transition metal based compounds, including oxides,[29] hydroxides,[30] sulfides,[31] phosphides,[32] selenides,[33] and nitrides[34] have been employed extensively as electrocatalysts for the OER in alkaline media. Among the MOF-derived metal oxides, Co-MOF derived  $\text{Co}_3\text{O}_4$  are getting special attention because of its carbon coated morphology.[35] It is interesting to note that although there are many MOF-based/derived electrocatalysts reported in recent years for the alkaline OER,[3,36,37] they are not yet to be explored for the acidic OER.

In addition to dissolution of electrocatalysts, it has been found that degradation of the substrate such as carbon cloth (CC) [22] as well as poor adhesion between the catalyst and the substrate such as Ti foils [38] also contribute to the failure of the electrodes in acidic OER. Hence, the selection of substrate is also critical for electrode development for acidic OER. In this regard, fluorine-doped tin oxide (FTO) glass, with its stability against high applied potentials ( $\sim 2.2$  V vs. RHE) in acidic media, is considered a suitable substrate for acidic OER.[39] On the other hand, binders are generally required to load electrocatalysts onto substrates to fabricate the electrodes. Unfortunately, most binders are polymeric materials and generally poor electrical conductors, using which tends to reduce the effective contact between the electrolyte and the active sites of the catalyst thereby decreasing the electrical conductivity of the fabricated electrode.[40] Because of the binders, the adhesion of the electrocatalysts on the substrates is often not sufficiently strong to withstand the mechanical stresses created during the oxygen evolution, leading to mechanical instability of the electrode over the long run.[41] In this regard, direct growth of electrocatalysts on conductive substrates enables better adhesion of the electrocatalysts with the substrates thereby improving the charge transport and mechanical stability of the resulting electrodes.[42,43] Most importantly,

the issues of active site blockage and poor electrical conductivity arising from the use of binders can be avoided.

Based on the above considerations, herein, we report a simple strategy to synthesize an in situ grown, Co-MOF-derived, carbon coated and Fe-doped spinel  $\text{Co}_3\text{O}_4$  (Fe- $\text{Co}_3\text{O}_4$ @C) catalyst on an FTO glass, Fe- $\text{Co}_3\text{O}_4$ @C/FTO, that is active and stable for catalyzation of the OER in acidic media. A Co-MOF was first grown in-situ on an FTO glass to serve as the precursor for fabrication of the desired Fe- $\text{Co}_3\text{O}_4$ @C/FTO through a simple thermal treatment as illustrated in Fig. 1. The Fe- $\text{Co}_3\text{O}_4$ @C/FTO electrode exhibited good OER performances with a low overpotential of 396 mV to achieve the current density of  $10 \text{ mA cm}^{-2}$  and a low Tafel slope of  $68.6 \text{ mV dec}^{-1}$  in  $0.5 \text{ M H}_2\text{SO}_4$ . Furthermore, electrochemical performances of Fe- $\text{Co}_3\text{O}_4$ @C/FTO remained stable for over 50 h at  $10 \text{ mA cm}^{-2}$ .

## 2. Experimental section

### 2.1. Chemicals

Cobalt(II) nitrate hexahydrate ( $\text{Co}(\text{NO}_3)_2 \cdot 6\text{H}_2\text{O}$ , 97.7%), 2-aminoterephthalic acid ( $\text{H}_2\text{BDC-NH}_2$ , 99%), iridium(IV) oxide ( $\text{IrO}_2$ , 99%), and sulfuric acid (95.0–98.0%) were purchased from Alfa Aesar. Ultrapure deionized water (DI water,  $\sim 18 \text{ M}\Omega$ ) was used for all the experiments, which was produced with a Milli-Q® Advantage A10 Water Purification System. All other chemicals and reagents were of analytical grade and used as received without further purification. Commercially available fluorine-doped tin oxide (FTO) coated glass ( $4 \text{ cm} \times 1 \text{ cm}$ ; thickness:  $2.2 \text{ mm}$ ; resistance:  $5\text{--}7 \Omega$ ) was purchased from Ruilong Optoelectronics (Miaoli County 356, Taiwan). To activate the FTO surface, the FTO glass was ultrasonicated in a solution containing  $30 \text{ mL}$  of  $3 \text{ M HCl}$  and  $150 \mu\text{L}$  of  $\text{HF}$  for  $30 \text{ min}$ , and then washed thoroughly with DI water three times and drying at  $50^\circ\text{C}$  for  $30 \text{ min}$  in a vacuum oven.

### 2.2. Electrode fabrications

#### 2.2.1. Growth of Co-MOF on FTO glass surface

The pre-treated FTO glass was placed in a  $100 \text{ mL}$  Teflon-lined bomb, with an inclined angle of  $\sim 30^\circ$  and its conducting side facing up, submerging in a solution containing DMF ( $35 \text{ mL}$ ), ethanol ( $2.5 \text{ mL}$ ), DI water ( $2.5 \text{ mL}$ ),  $\text{Co}(\text{NO}_3)_2 \cdot 6\text{H}_2\text{O}$  ( $1.5 \text{ mmol}$ ), 2-aminoterephthalic acid ( $1.5 \text{ mmol}$ ), and  $\text{HF}$  ( $75 \mu\text{L}$ ). The solvothermal reaction was conducted at  $150^\circ\text{C}$  for  $2 \text{ h}$  to grow Co-MOF on the FTO glass substrate. The product, named as Co-MOF/FTO, was washed with 95% aqueous ethanol and dried in an oven at  $60^\circ\text{C}$  for later use. The mass loading of MOF on the FTO glass was found to be  $\sim 2.5 \text{ mg cm}^{-2}$ .

#### 2.2.2. Preparation of $\text{Co}_3\text{O}_4$ @C/FTO

Product Co-MOF/FTO was calcined in air at  $400^\circ\text{C}$  for  $1 \text{ h}$  with a heating rate of  $3^\circ\text{C min}^{-1}$  to convert Co-MOF into carbon coated  $\text{Co}_3\text{O}_4$  to afford  $\text{Co}_3\text{O}_4$ @C/FTO. The mass loading of  $\text{Co}_3\text{O}_4$ @C on the FTO glass substrate was measured to be  $\sim 1.1 \text{ mg cm}^{-2}$ .

#### 2.2.3. Fe doping process

Two mg ( $0.01 \text{ mmol}$ ) of  $\text{FeCl}_2 \cdot 4\text{H}_2\text{O}$  was dissolved in  $1 \text{ mL}$  of 95%

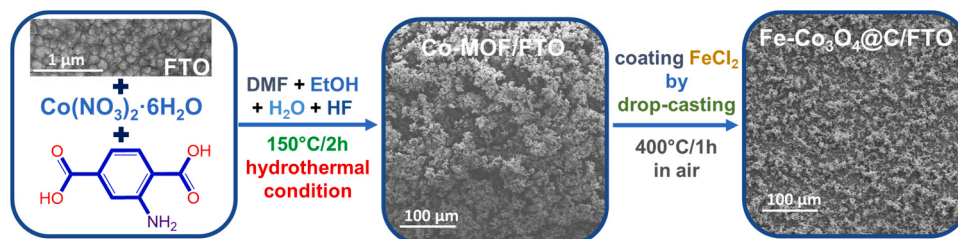


Fig. 1. Synthetic process of Co-MOF and Fe- $\text{Co}_3\text{O}_4$ @C on FTO.

ethanol. From the stock solution, 50  $\mu\text{L}$  was drop-casted on Co-MOF/FTO ( $1\text{ cm}^2$ ) evenly and then dried at room temperature for 1 h. The Fe precursor containing Co-MOF/FTO was calcined in air at  $400\text{ }^\circ\text{C}$  for 1 h (heating rate:  $3\text{ }^\circ\text{C min}^{-1}$ ) to convert the Fe precursor containing Co-MOF into carbon coated Fe-doped  $\text{Co}_3\text{O}_4$  to afford Fe- $\text{Co}_3\text{O}_4$ @C/FTO. The mass loading of Fe- $\text{Co}_3\text{O}_4$ @C on the FTO glass substrate was measured to be  $\sim 1.1\text{ mg cm}^{-2}$ .

#### 2.2.4. Fabrication of bulk $\text{Co}_3\text{O}_4$ @C/FTO and $\text{Co}_3\text{O}_4$ /FTO electrodes

For comparison purposes, bulk  $\text{Co}_3\text{O}_4$ @C/FTO and  $\text{Co}_3\text{O}_4$ /FTO electrodes were also fabricated. Twenty five mg of bulk Co-MOF, synthesized with the same procedures for Co-MOF/FTO but without the presence of the FTO glass, was well dispersed in 1 mL of 95% ethanol under ultrasonication for 30 min. One hundred  $\mu\text{L}$  of the ink-like stock dispersion was drop-casted on an FTO glass ( $1\text{ cm}^2$ ) evenly and then dried at  $60\text{ }^\circ\text{C}$  for 5 h. The obtained bulk Co-MOF/FTO was then calcined at  $400\text{ }^\circ\text{C}$  for 1 h to afford the bulk  $\text{Co}_3\text{O}_4$ @C/FTO electrode. For the  $\text{Co}_3\text{O}_4$ /FTO electrode, 100  $\mu\text{L}$  of  $\text{Co}(\text{NO}_3)_2 \cdot 6\text{H}_2\text{O}$  solution (13.3 mg in 1 mL of 95% ethanol) was drop-casted onto an FTO glass ( $1\text{ cm}^2$ ), followed by drying at  $60\text{ }^\circ\text{C}$  for 5 h and subsequent calcination in air at  $400\text{ }^\circ\text{C}$  for 1 h. The mass loading of both bulk  $\text{Co}_3\text{O}_4$ @C and  $\text{Co}_3\text{O}_4$  on FTO was controlled to be  $\sim 1.1\text{ mg cm}^{-2}$ .

#### 2.2.5. Fabrication of $\text{IrO}_2$ /FTO electrode

For the fabrication of the  $\text{IrO}_2$ /FTO electrode, 22 mg of  $\text{IrO}_2$  sample was dispersed in 1.0 mL of 0.75 wt% Nafion solution in isopropyl alcohol (IPA). The dispersion was sonicated for 30 min to form a homogeneous ink. Fifty  $\mu\text{L}$  of the dispersion was drop-casted onto an FTO glass ( $1 \times 1\text{ cm}^2$ ) with an  $\text{IrO}_2$  mass loading of  $1.1\text{ mg cm}^{-2}$ , same as those of other electrodes for fair comparison, followed by drying at  $60\text{ }^\circ\text{C}$  for 5 h.

### 2.3. Characterization

A field emission scanning electron microscope (FE-SEM, Hitachi S-4800, Hitachi High-Technologies Corporation, Japan) was used to record the morphology of the materials grown on FTO. High resolution transmission electron microscope (HR-TEM) images of MOF-derived materials scratched off from the corresponding FTO glass surface were collected from an HR-TEM instrument (JEOL 205 3000 F, JEOL Ltd.) The energy dispersive X-ray (EDX) spectroscopy (Max N 100TLE, Oxford Instruments plc) equipped with a TEM was used to analyze the elemental composition and distribution of the synthesized electrocatalysts. The powder XRD patterns of the synthesized samples were carried out with an X-ray diffractometer (D8 ADVANCE Eco, Bruker Corp.), having Cu K $\alpha$  radiations as the X-ray source. A surface area analyzer (ASAP 2010, Micromeritics Inc., Norcross, GA) was employed for measurements of  $\text{N}_2$  adsorption/desorption isotherms. The specific surface areas of the MOF-derived samples were determined based on the Brunauer-Emmett-Teller (BET) model. The metallic elements in the MOF-derived samples were quantified by using inductively coupled plasma with optical emission spectrometry (ICP-OES, iCAP 7000 series, Thermo Fisher Scientific). High resolution X-ray photoelectron spectroscopy (HR-XPS) spectra for all the synthesized samples and the tested electrodes after stability tests were obtained with a high-resolution X-ray photoelectron spectrometer (Thermo ESCALAB 250XI, USA) using a scanning X-ray microprobe equipped with an Al anode as the excitation source. For determination of Faradaic efficiency, the gas collected during the OER process was analyzed with a gas chromatography (GC-2014, SHIMADZU) equipped with a thermal conductivity detector.

### 2.4. Electrochemical measurements

The OER electrocatalytic properties of the fabricated FTO electrodes (geometric area:  $1\text{ cm} \times 1\text{ cm}$ ) were assessed in an electrochemical workstation (CHI6275D) of a three-electrode system in 0.5 M  $\text{H}_2\text{SO}_4$

(pH  $\sim 0.3$ ) at  $25\text{ }^\circ\text{C}$ . The FTO electrode served as the working electrode along with Ag/AgCl (0.210 V vs. normal hydrogen electrode, NHE) and platinum foil ( $1 \times 1\text{ cm}^2$ ) serving as the reference and counter electrodes, respectively. Prior to use, all working electrodes were conditioned to produce stable currents by cycling them ten times with cyclic voltammetry (CV) in a potential range of 0.90–1.80 V (vs. reversible hydrogen electrode, RHE) at a scan rate of  $100\text{ mV s}^{-1}$  in 0.5 M  $\text{H}_2\text{SO}_4$ . The linear sweep voltammetry (LSV) was performed at a slow scan rate of  $1\text{ mV s}^{-1}$  with iR compensation for all sample electrodes. The reported potentials for the OER were referenced to RHE by using the Nernst equation,  $E_{\text{RHE}} = (E_{\text{Ag/AgCl}} + 0.210 + 0.059 \times \text{pH})\text{ V}$ . And, the overpotential ( $\eta$ ) values were calculated by using the equation:  $\eta = (E_{\text{RHE}} - 1.23)\text{ V}$ . Electrochemical impedance spectroscopy (EIS) measurements were carried out for all electrodes with the applied frequency ranging from  $10^5\text{ Hz}$  to  $10^{-2}\text{ Hz}$  at a fixed operating potential of 1.75 V (vs. RHE). Faradaic efficiency of Fe- $\text{Co}_3\text{O}_4$ @C/FTO for the OER was determined by comparing the numbers of moles of oxygen produced experimentally and calculated theoretically. The theoretical number of moles of oxygen produced ( $N_T$ ) was calculated by using the following equation,  $N_T = (i \times t)/4F$ , where  $i$  is the current recorded,  $t$  is the time, and  $F$  is the Faraday constant. The amount of oxygen produced experimentally ( $N_E$ ) was measured with the water displacement method [44].

## 3. Results and Discussion

### 3.1. Materials characterizations

The Co-MOF was grown in situ on the surface of an FTO glass with a one-step solvothermal process ( $150\text{ }^\circ\text{C}/2\text{ h}$ ), using  $\text{H}_2\text{BDC-NH}_2$  as the organic ligand and  $\text{Co}(\text{NO}_3)_2 \cdot 6\text{H}_2\text{O}$  as the cobalt source as illustrated in Fig. 1 and described in the experimental section. The Co-MOF appears to grow as micro-sized particles and fully cover the FTO glass as evident from the SEM images (Fig. S1, Supporting Information). And it is composed of Co, C, N, O, and F as judged from the SEM-EDX measurement (Fig. S2, Supporting Information), in which Co is the metal center, C, N, and O are from the organic ligand, and F is from the solvent to coordinate with the metal ion to maintain charge neutrality of the Co-MOF. Fig. S3 (Supporting Information) shows the XRD pattern of the Co-MOF scratched off from Co-MOF/FTO, which is in good agreement with that of the Co-MOF reported in our previous work.[45] Furthermore, the full survey XPS spectrum of Co-MOF/FTO (Fig. S4a, Supporting Information) confirms again the presence of Co, C, N, O, and F in Co-MOF. The HR-XPS spectrum of Co2p of Co-MOF/FTO (Fig. S4b, Supporting Information) displays the binding energy peaks at 780.2 and 796.2 eV for Co2p $_{3/2}$  and Co2p $_{1/2}$ , respectively, indicating that the cobalt ions present in the Co-MOF are in +2 oxidation [46].

The Co-MOF was thermally converted to the desired carbon coated cobalt oxide at calcination of  $400\text{ }^\circ\text{C}$  in air for 1 h, with the product named as  $\text{Co}_3\text{O}_4$ @C/FTO. As for the Fe-doped  $\text{Co}_3\text{O}_4$ , an Fe precursor was introduced to the Co-MOF before the calcination and the product was named as Fe- $\text{Co}_3\text{O}_4$ @C/FTO. The morphologies of  $\text{Co}_3\text{O}_4$ @C/FTO and Fe- $\text{Co}_3\text{O}_4$ @C/FTO were observed with SEM as shown in Fig. 2a-h in a zoom-in sequence. Both products cover the FTO glass fully and densely (Fig. 2a and b) with micron-sized particles (Fig. 2c-f). These micron-sized particles resemble those of Co-MOF in shape and size, and are in fact aggregates of primary particles of 10–20 nm (Fig. 2g & h). The observation implies that the Co-MOF particles maintain their shape and size during the thermal conversion process and the breakage of organic ligands and subsequent release of gaseous side products limit the crystal growth of  $\text{Co}_3\text{O}_4$  to be in nanoscale. Interestingly, if examined closely, the primary particle size of Fe- $\text{Co}_3\text{O}_4$ @C is significantly smaller than that of  $\text{Co}_3\text{O}_4$ @C (Fig. 2g & h), implying that the presence of the Fe precursor and subsequent Fe-dopant impede further growth of  $\text{Co}_3\text{O}_4$  crystals, resulting in smaller sized primary particles. Further, the atomic ratio of Fe:Co was determined to be 1:49 for Fe- $\text{Co}_3\text{O}_4$ @C based on the SEM-EDX data of Fe- $\text{Co}_3\text{O}_4$ @C/FTO (Fig. 2i).



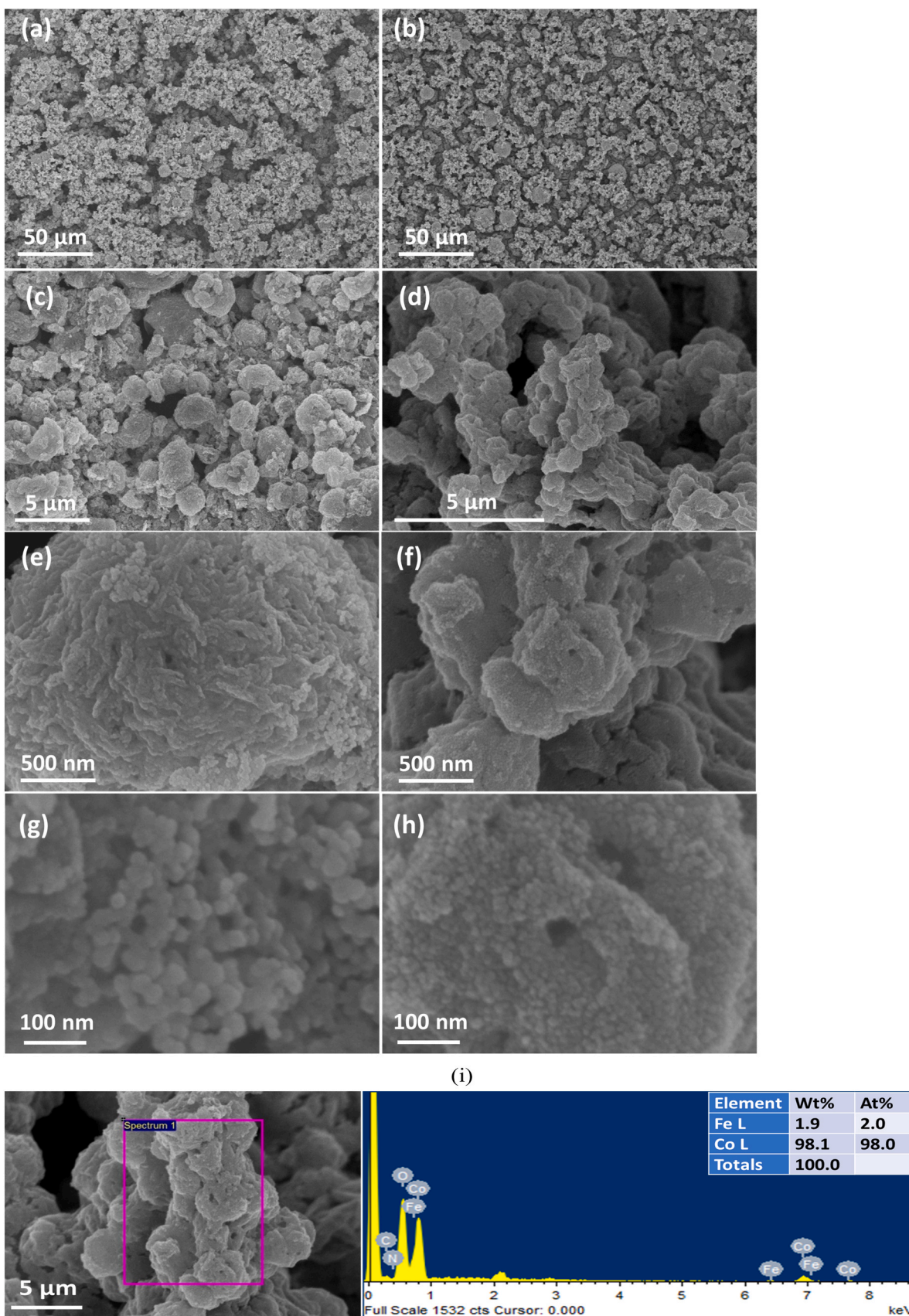


Fig. 2. SEM images of  $\text{Co}_3\text{O}_4/\text{C}/\text{FTO}$  (a, c, e & g) and  $\text{Fe-Co}_3\text{O}_4/\text{C}/\text{FTO}$  (b, d, f & h) at increasing resolutions. (i) SEM-EDX result of  $\text{Fe-Co}_3\text{O}_4/\text{C}/\text{FTO}$ .



The size reduction in primary  $\text{Co}_3\text{O}_4$  nanoparticles associated with the Fe-doping can be further confirmed with the TEM images of  $\text{Co}_3\text{O}_4/\text{C}$  (Fig. 3a) and  $\text{Fe-Co}_3\text{O}_4/\text{C}$  (Fig. 3c) scratched off from  $\text{Co}_3\text{O}_4/\text{C}/\text{FTO}$  and  $\text{Fe-Co}_3\text{O}_4/\text{C}/\text{FTO}$ , respectively. The size distributions of  $\text{Co}_3\text{O}_4/\text{C}$  and  $\text{Fe-Co}_3\text{O}_4/\text{C}$  as compiled from the TEM images are  $18.8 \pm 2.6$  and  $13.2 \pm 2.3$  nm, respectively, significantly different with an average size difference of more than 5 nm, confirming the inhibition effect of Fe-doping toward crystal growth of  $\text{Co}_3\text{O}_4$ . Furthermore, for  $\text{Co}_3\text{O}_4/\text{C}$ , two interlayer distances of 0.28 and 0.23 nm are determined from the HR-TEM image shown in Fig. 3b, corresponding well to the lattice spacing of crystalline planes (220) and (222), respectively of  $\text{Co}_3\text{O}_4$ . [23] As to  $\text{Fe-Co}_3\text{O}_4/\text{C}$ , two interlayer distances of 0.28 and 0.47 nm are obtained from Fig. 3d, in good agreement with the d-spacing of crystalline planes (220) and (111) of  $\text{Co}_3\text{O}_4$ . [23] Both pairs of crystalline planes contain an angle of  $90^\circ$  as they should. Also important to note is that both  $\text{Co}_3\text{O}_4$  and  $\text{Fe-Co}_3\text{O}_4$  nanoparticles are coated with thin layers of amorphous carbons as evident from the HR-TEM images shown in Fig. S5 (Supporting Information), confirming the core-shell structure of both  $\text{Co}_3\text{O}_4/\text{C}$  and  $\text{Fe-Co}_3\text{O}_4/\text{C}$ . The carbon coating is beneficial to the electrocatalytic performances of  $\text{Co}_3\text{O}_4$  through improving the overall charge transport of the electrode and serving as a protective layer to enhance the electrocatalytic stability of  $\text{Co}_3\text{O}_4$ . Furthermore, the TEM-EDX elemental mapping of  $\text{Fe-Co}_3\text{O}_4/\text{C}$  (Fig. 3e) reveals that the constituent elements, Co, Fe, O, and C are homogeneously distributed in the sample. Moreover, the TEM-EDX data of  $\text{Fe-Co}_3\text{O}_4/\text{C}$  (Fig. 3f) are consistent with the corresponding SEM-EDX data and the atomic ratio of Fe vs. Co in  $\text{Fe-Co}_3\text{O}_4/\text{C}$  is about 1:52, close to 1:49 determined by the SEM-EDX data.

The amounts of metallic elements, Co and Fe, present in  $\text{Co}_3\text{O}_4/\text{C}$  and  $\text{Fe-Co}_3\text{O}_4/\text{C}$  can be more accurately determined with ICP-OES, from which the atomic ratio of Fe vs. Co in  $\text{Fe-Co}_3\text{O}_4/\text{C}$  and the weight percent of carbon in both samples can be estimated. The results are tabulated in Table S1 (Supporting Information). The atomic ratio of Fe vs. Co in  $\text{Fe-Co}_3\text{O}_4/\text{C}$  is 1:54, in good agreement with that determined from TEM-EDX, 1:52. The carbon remaining in  $\text{Co}_3\text{O}_4/\text{C}$  and  $\text{Fe-Co}_3\text{O}_4/\text{C}$  are estimated to be 18.0 and 19.3 wt%, respectively. The crystalline structure of  $\text{Co}_3\text{O}_4/\text{C}$  and  $\text{Fe-Co}_3\text{O}_4/\text{C}$  were confirmed with powder XRD as shown in Fig. 4a. The XRD patterns matched well with that of the cubic phase of  $\text{Co}_3\text{O}_4$  (JCPDS # 42-1467), and there are no additional impurity diffraction peaks, indicating the sole crystalline product of  $\text{Co}_3\text{O}_4$ . If examined closely, the diffraction peaks of  $\text{Fe-Co}_3\text{O}_4/\text{C}$  are slightly left shifted as compared with the corresponding diffraction peaks of  $\text{Co}_3\text{O}_4/\text{C}$  (inset of Fig. 4a), indicating the slight lattice expansion caused by the doping of Fe, whose atomic size is slightly larger than that of Co. It is interesting to note that, although both samples contain considerable amounts of carbon, no characteristic diffraction peaks of carbon are detected with the powder XRD, confirming the amorphous nature of the carbon coating. Furthermore, the grain sizes of  $\text{Co}_3\text{O}_4$  and  $\text{Fe-Co}_3\text{O}_4$  were estimated with the Scherrer equation, based on the diffraction peak (311), to be 20.5 and 14.1 nm, respectively, which matched well with the corresponding primary particle sizes of the two samples determined from the HR-TEM imaging, implying that the primary particles are likely to be single crystalline. To further investigate the atomic compositions and chemical states of the samples, X-ray photoelectron spectroscopy (XPS) were conducted. As shown in Fig. 4b, all constituent elements of  $\text{Co}_3\text{O}_4/\text{C}$ , Co, O, and C, are present in the sample. Fig. 4c shows the high resolution XPS spectrum of Co2p, in which characteristic binding energies (B.E.) of 778.5 and 793.7 eV are identified, attributable to  $\text{Co}2p_{3/2}$  and  $\text{Co}2p_{1/2}$  of  $\text{Co(III)}$  species, respectively, whereas the peaks at 780.0 and 795.5 eV correspond to  $\text{Co}2p_{3/2}$  and  $\text{Co}2p_{1/2}$  of  $\text{Co(II)}$  species, respectively [47].

The full survey XPS spectrum (Fig. 4d) of  $\text{Fe-Co}_3\text{O}_4/\text{C}$  shows the presence of all constituent elements of  $\text{Fe-Co}_3\text{O}_4/\text{C}$ , including Fe, Co, O, and C. The HR-XPS spectrum of Co2p of  $\text{Fe-Co}_3\text{O}_4/\text{C}/\text{FTO}$  (Fig. 4e) identifies the binding energy peaks of  $\text{Co}2p_{3/2}$  and  $\text{Co}2p_{1/2}$  of  $\text{Co}^{3+}$  species at 778.9 and 794.2 eV, respectively, and the signals at 780.5 and

796.0 eV correspond to  $\text{Co}2p_{3/2}$  and  $\text{Co}2p_{1/2}$  of  $\text{Co}^{2+}$  species, respectively. [47] It is worth noting that, with Fe doping, the Co peaks shift higher in binding energy by an amount of 0.4 eV, indicating modulation of the electronic structure of  $\text{Co}_3\text{O}_4$  with Fe-doping. The upshifts in binding energies for  $\text{Co}^{2+}$  and  $\text{Co}^{3+}$  indicate increased electron deficiency of both  $\text{Co}^{2+}$  and  $\text{Co}^{3+}$ , which is beneficial for catalyzation of oxidative reactions. It has been reported that electron-deficient Co sites in  $\text{Co}_3\text{O}_4$  may enhance its OER activities. [23] For Fe2p, the binding energy peak located at 711.2 eV corresponds to  $\text{Fe}2p_{3/2}$  (Fig. 4f) and suggests that the Fe ion exists in the 3+ oxidation state. [23] Fig. 4g displays the  $\text{N}_2$  adsorption/desorption isotherms of  $\text{Co}_3\text{O}_4/\text{C}$  and  $\text{Fe-Co}_3\text{O}_4/\text{C}$ , from which the specific surface areas of  $\text{Co}_3\text{O}_4/\text{C}$  and  $\text{Fe-Co}_3\text{O}_4/\text{C}$  are determined to be 29.3 and 35.0  $\text{m}^2 \text{g}^{-1}$ , respectively. As expected,  $\text{Fe-Co}_3\text{O}_4/\text{C}$  possesses a higher specific surface area than  $\text{Co}_3\text{O}_4/\text{C}$ , attributable to the size reduction in primary particles induced by Fe-doping. The higher surface area of  $\text{Fe-Co}_3\text{O}_4/\text{C}$  is advantageous to offer more active sites for catalyzation of the OER. In conclusion, Fe-doping leads to increased electron deficiency of Co sites and exposure of more active sites of  $\text{Co}_3\text{O}_4$  than the non-doped one, both favorable for enhanced OER performances.

### 3.2. Evaluation of OER electrocatalytic properties

#### 3.2.1. LSV measurements

The OER performances of the fabricated electrodes namely, the blank FTO,  $\text{IrO}_2/\text{FTO}$ ,  $\text{Co}_3\text{O}_4/\text{C}/\text{FTO}$ , and  $\text{Fe-Co}_3\text{O}_4/\text{C}/\text{FTO}$ , were assessed in a strong acidic medium, 0.5 M  $\text{H}_2\text{SO}_4$  having the pH value of  $\sim 0.3$ . First, LSV measurements are conducted and the resulting LSV polarization curves are presented in Fig. 5a-b, with the corresponding overpotentials at the current density of 10  $\text{mA cm}^{-2}$  ( $\eta_{10}$ ) marked for comparison. It is important to note that a slow scan rate of 1  $\text{mV s}^{-1}$  has been applied for all LSV measurements to avoid the interference of the induced capacitive currents. As shown in Fig. 5a, the OER efficiency of  $\text{Fe-Co}_3\text{O}_4/\text{C}/\text{FTO}$  is enhanced with the Fe-doping, decreasing  $\eta_{10}$  from 422 mV achieved by  $\text{Co}_3\text{O}_4/\text{C}/\text{FTO}$  to 396 mV. Both  $\text{Co}_3\text{O}_4/\text{C}/\text{FTO}$  and  $\text{Fe-Co}_3\text{O}_4/\text{C}/\text{FTO}$  outperform the blank FTO electrode (Fig. 5b,  $\eta_{10} = 1485$  mV) by a huge extent, proving that  $\text{Co}_3\text{O}_4/\text{C}$  and  $\text{Fe-Co}_3\text{O}_4/\text{C}$  are the active materials of the electrodes toward catalyzation of the OER and the contribution of the FTO glass substrate can be safely neglected. Although not as efficient as the noble metal based benchmark electrode  $\text{IrO}_2/\text{FTO}$  ( $\eta_{10} = 323$  mV),  $\eta_{10}$  of  $\text{Fe-Co}_3\text{O}_4/\text{C}/\text{FTO}$  is lower than many of the recently reported non-noble metal based OER electrocatalysts (all in 0.5 M  $\text{H}_2\text{SO}_4$ ), including  $\gamma\text{-MnO}_2$  ( $\eta_{10} = 428$  mV), [48]  $\text{Co}_3\text{O}_4/\text{FTO}$  ( $\eta_{10} = 570$  mV), [15] Ag-doped  $\text{Co}_3\text{O}_4$  ( $\eta_{10} = 470$  mV), [49]  $\text{Co}_{0.05}\text{Fe}_{0.95}\text{O}_y$  ( $\eta_{10} = 650$  mV), [50] 1 T  $\text{MoS}_2$  ( $\eta_{10} = 420$  mV), [51] and  $\text{Ni}_2\text{Ta}$  pellets ( $\eta_{10} = 570$  mV) [52]. Next, the Tafel slope values for the tested electrodes were determined to evaluate their OER kinetics. As observed in Fig. 5c-d,  $\text{Fe-Co}_3\text{O}_4/\text{C}/\text{FTO}$  displays the lowest Tafel slope value of 68.6  $\text{mV dec}^{-1}$  over the other three samples,  $\text{Co}_3\text{O}_4/\text{C}/\text{FTO}$  (99.1  $\text{mV dec}^{-1}$ ),  $\text{IrO}_2/\text{FTO}$  (126  $\text{mV dec}^{-1}$ ), and blank FTO (456  $\text{mV dec}^{-1}$ ), suggesting that  $\text{Fe-Co}_3\text{O}_4/\text{C}/\text{FTO}$  can readily reach high current densities at the expense of a small extra potential. In order to show the merits of carbon coating and in-situ growth of  $\text{Co}_3\text{O}_4$  on the OER performances, two comparison electrodes, namely  $\text{Co}_3\text{O}_4/\text{FTO}$  and bulk  $\text{Co}_3\text{O}_4/\text{C}/\text{FTO}$ , were fabricated to compete with  $\text{Co}_3\text{O}_4/\text{C}/\text{FTO}$ . Here,  $\text{Co}_3\text{O}_4/\text{FTO}$  is without carbon coating and bulk  $\text{Co}_3\text{O}_4/\text{C}/\text{FTO}$  is fabricated through casting  $\text{Co}_3\text{O}_4/\text{C}$  powders onto the FTO glass with the help of binders. The corresponding LSV curves and Tafel plot are presented in Fig. S6 (Supporting Information) and Fig. S7 (Supporting Information), respectively. Evidently, bulk  $\text{Co}_3\text{O}_4/\text{C}/\text{FTO}$  ( $\eta_{10} = 478$  mV; Tafel slope = 105  $\text{mV dec}^{-1}$ ) shows better OER performances than those of  $\text{Co}_3\text{O}_4/\text{FTO}$  ( $\eta_{10} = 545$  mV; Tafel slope = 116  $\text{mV dec}^{-1}$ ), revealing the benefit of carbon coating. Furthermore, the OER performances of bulk  $\text{Co}_3\text{O}_4/\text{C}/\text{FTO}$  are significantly inferior to those of  $\text{Co}_3\text{O}_4/\text{C}/\text{FTO}$ , witnessing the advantages of in-situ grown and thus binder-free electrodes.

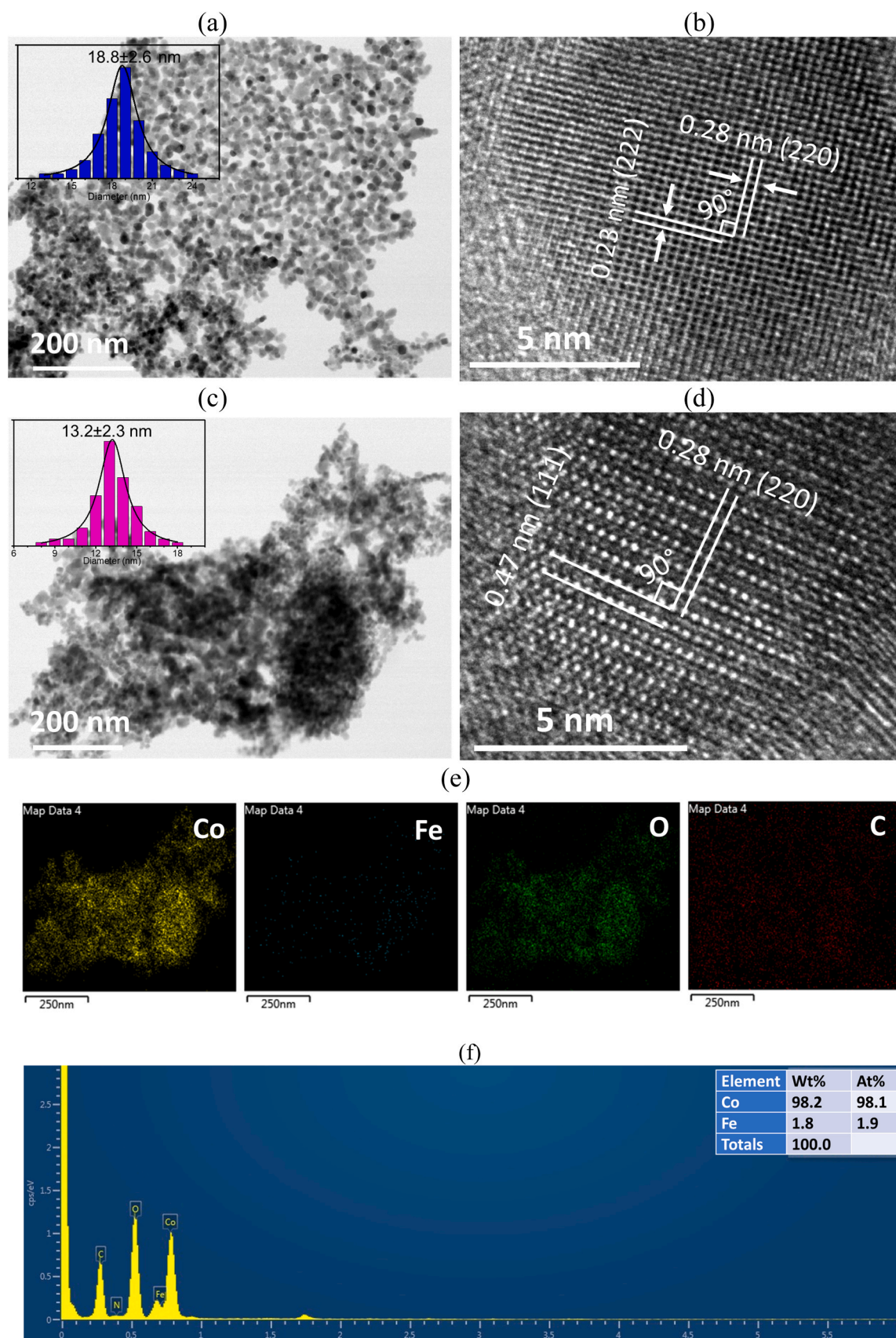


**Fig. 3.** (a) TEM and (b) HR-TEM images of  $\text{Co}_3\text{O}_4@\text{C}$ . (c) TEM and (d) HR-TEM images of  $\text{Fe-Co}_3\text{O}_4@\text{C}$ . (e) TEM-EDX mapping of Co, O, C, and Fe in  $\text{Fe-Co}_3\text{O}_4@\text{C}$ . (f) TEM-EDX measurement of  $\text{Fe-Co}_3\text{O}_4@\text{C}$ .

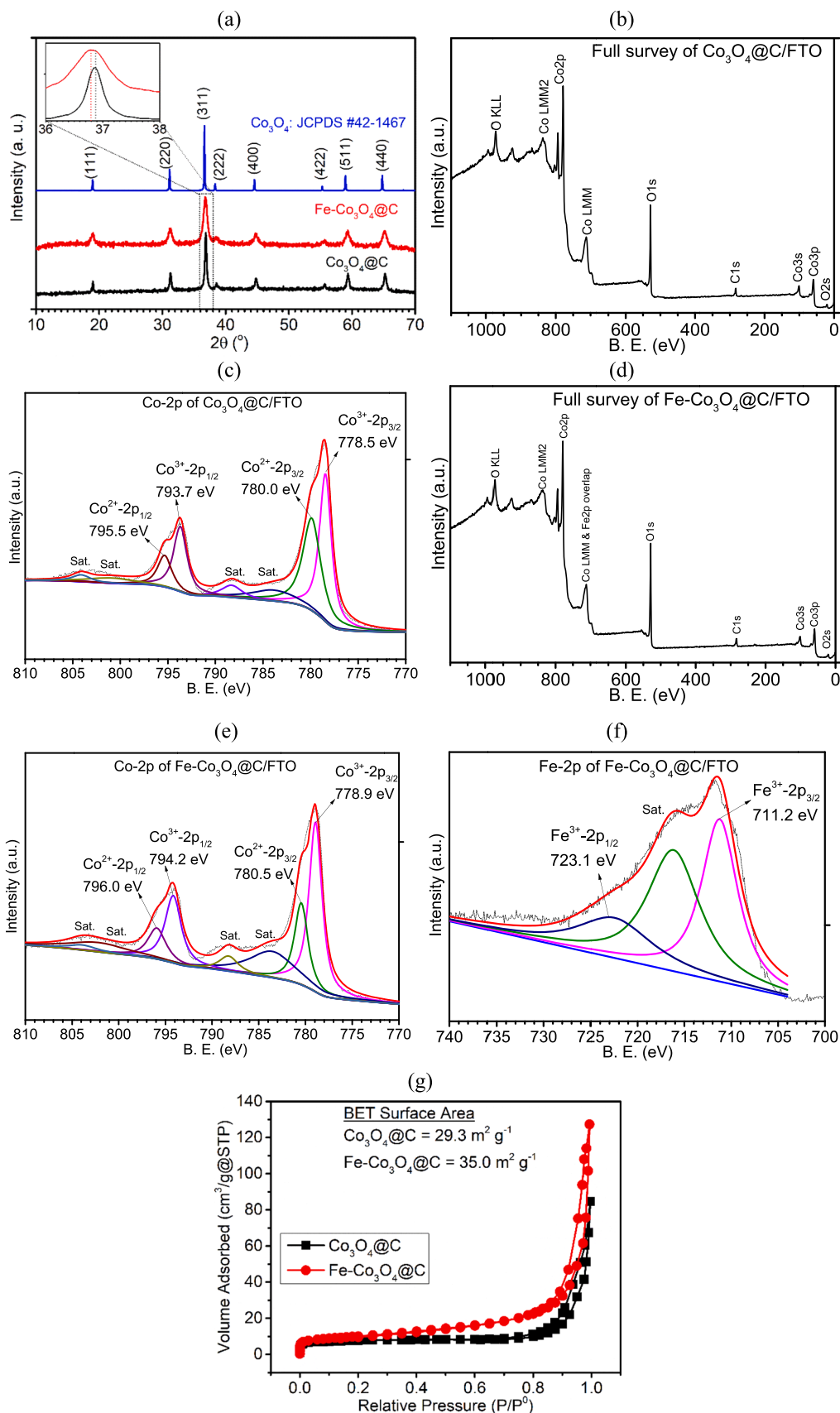


**Fig. 4.** (a) Powder XRD patterns of  $\text{Co}_3\text{O}_4$ @C and  $\text{Fe-Co}_3\text{O}_4$ @C scratched off from  $\text{Co}_3\text{O}_4$ @C/FTO and  $\text{Fe-Co}_3\text{O}_4$ @C/FTO, respectively. XPS spectra of  $\text{Co}_3\text{O}_4$ @C/FTO: (b) full survey and (c) HR-XPS of Co 2p; and  $\text{Fe-Co}_3\text{O}_4$ @C/FTO: (d) full survey, (e) HR-XPS of Co 2p, and (f) HR-XPS of Fe 2p. (g)  $\text{N}_2$  adsorption/desorption isotherms of  $\text{Co}_3\text{O}_4$ @C and  $\text{Fe-Co}_3\text{O}_4$ @C scratched off from  $\text{Co}_3\text{O}_4$ @C/FTO and  $\text{Fe-Co}_3\text{O}_4$ @C/FTO, respectively.



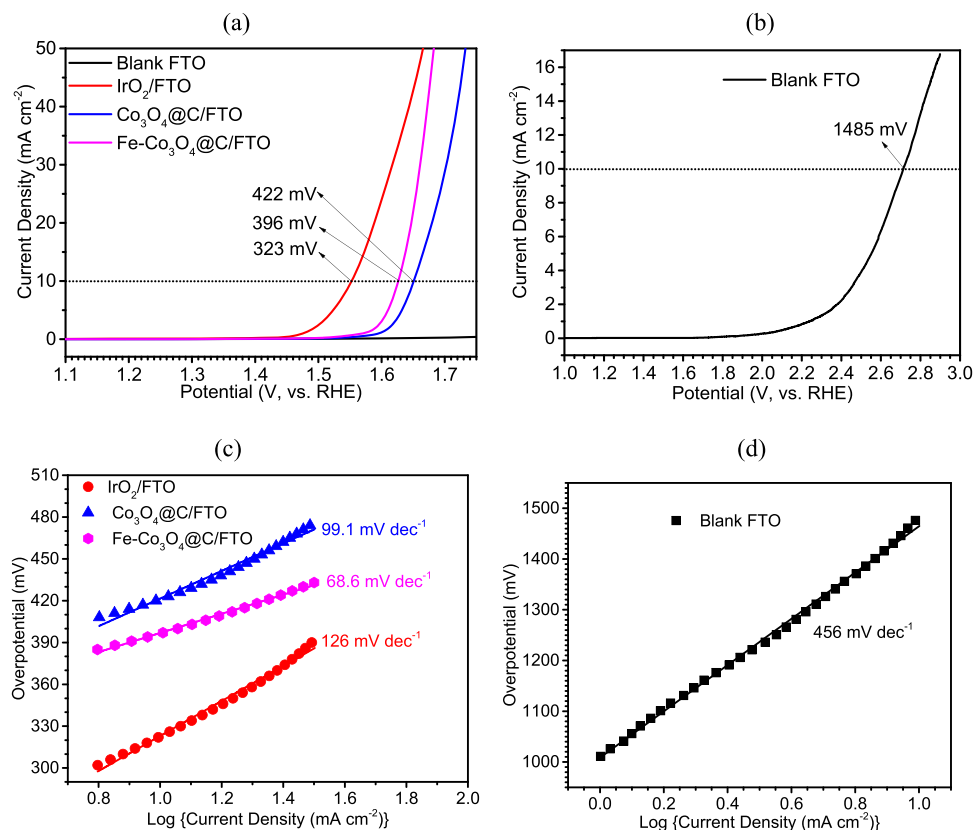


Fig. 5. (a,b) LSV polarization curves recorded in 0.5 M H<sub>2</sub>SO<sub>4</sub> at scan rate of 1 mV s<sup>-1</sup>, with (c,d) for corresponding Tafel plots.

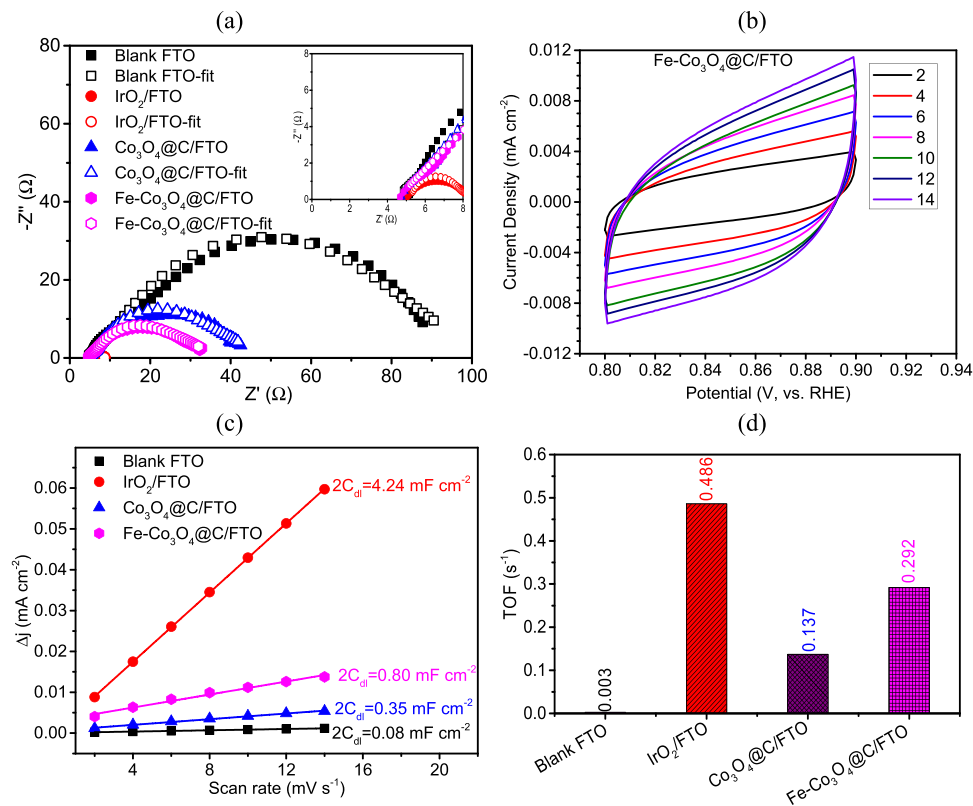


Fig. 6. (a) EIS-Nyquist plot of sample electrodes. (b) CV curves of Fe-Co<sub>3</sub>O<sub>4</sub>@C/FTO electrode at increasing scan rates (mV s<sup>-1</sup>). (c) Plot of current density difference (Δj) at 0.90 V (vs. RHE) against scan rate for estimation of double layer capacitance (C<sub>dl</sub>). (d) Turnover frequencies (TOFs) of OER of sample electrocatalysts estimated at 1.67 V (vs. RHE).

### 3.2.2. EIS, ECSA and TOF measurements

The electrochemical impedance spectroscopy (EIS) was then used to study the OER kinetics of the sample electrodes. The impedance was measured in 0.5 M  $\text{H}_2\text{SO}_4$  in the frequency range of 100 kHz to 10 mHz at a fixed applied potential of 1.75 V (vs. RHE), with which all electrocatalysts proceed with the OER. The corresponding Nyquist plots (Fig. 6a) are fitted with an equivalent circuit model (Fig. S8, Supporting Information) to extract the charge transfer resistance ( $R_{ct}$ ) values. Accordingly, the  $R_{ct}$  values are determined to be 2.2, 7.8, 14.0, and 38.3  $\Omega$  for  $\text{IrO}_2/\text{FTO}$ ,  $\text{Fe-Co}_3\text{O}_4/\text{C}/\text{FTO}$ ,  $\text{Co}_3\text{O}_4/\text{C}/\text{FTO}$ , and blank FTO, respectively, consistent with the trend observed in  $\eta_{10}$ . It is evident that Fe-doping enhances the interfacial charge transfer efficiency of  $\text{Co}_3\text{O}_4$ , reducing the  $R_{ct}$  value from 14.0  $\Omega$  for  $\text{Co}_3\text{O}_4/\text{C}/\text{FTO}$  to 7.8  $\Omega$  for  $\text{Fe-Co}_3\text{O}_4/\text{C}/\text{FTO}$ .

Furthermore, the OER efficacy of all tested samples is investigated in terms of the electrochemical surface area (ECSA). It is well-established that the catalytic performance of an electrocatalyst is dependent on the quantity of its active sites as well as the intrinsic activity of its exposed active sites. In this regard, ECSA serves as a direct parameter to quantify the exposed active sites. ECSA can be estimated by dividing the double layer capacitance ( $C_{dl}$ ) of the catalyst with a reference specific capacitance ( $C_s$ ). The  $C_{dl}$  values of the samples are first determined. CV curves were first recorded for all tested electrodes to estimate their  $C_{dl}$  values with increasing scan rates of 2, 4, 6, 8, 10, 12, and 14  $\text{mV s}^{-1}$  in the potential range of 0.85–0.95 V (vs. RHE), in which only non-Faradaic adsorption/desorption of electrolyte ions occurs. The corresponding CV plots for blank FTO,  $\text{IrO}_2/\text{FTO}$ ,  $\text{Co}_3\text{O}_4/\text{C}/\text{FTO}$ , and  $\text{Fe-Co}_3\text{O}_4/\text{C}/\text{FTO}$  are given in Figs. S9, S10, S11 (Supporting Information), and Fig. 6b respectively. The  $C_{dl}$  value was then determined by using the slope ( $C_{dl} = \text{slope}/2$ ) of the current density difference ( $\Delta j$ ) (at 0.90 V vs. RHE) versus scan rate (Fig. 6c) curves and the obtained  $C_{dl}$  values are marked in the plot. The corresponding ECSA values for all sample electrodes are determined by dividing their  $C_{dl}$  values with a commonly accepted  $C_s$  value of 0.040  $\text{mF cm}^{-2}$ . [53] The ECSA values are found to be 1.0, 53, 4.4, and 10  $\text{cm}^2$  for blank FTO,  $\text{IrO}_2/\text{FTO}$ ,  $\text{Co}_3\text{O}_4/\text{C}/\text{FTO}$ , and  $\text{Fe-Co}_3\text{O}_4/\text{C}/\text{FTO}$ , respectively. The trend is the same with that of overpotentials,  $\text{IrO}_2/\text{FTO}$  the best and blank FTO the worst. Note that Fe-doping reduces the grain and primary particle sizes of  $\text{Co}_3\text{O}_4$  as discussed earlier, giving a larger specific surface area and also ECSA for  $\text{Fe-Co}_3\text{O}_4/\text{C}$  over  $\text{Co}_3\text{O}_4/\text{C}$ .

In addition to ECSA, turnover frequency (TOF) is also an essential parameter to study the electrocatalytic water splitting efficiency, by providing the quality (intrinsic activity) of the active sites present in the electrocatalyst. The TOF values represent the number of oxygen molecules produced by an active site in one second. At a specific applied potential, the number of oxygen molecules produced per second can be estimated from the current density generated during the application of that specific applied potential, under the assumption of a 100% Faradaic efficiency. Further, a reduction peak area approach as reported in literature [54] was adopted to estimate the number of surface active sites for estimation of the TOF. Here, the TOF is specifically defined as the number of oxygen turnovers at 1.67 V (vs. RHE) divided by the number of the surface active sites. The obtained TOFs values for all electrodes are given in Fig. 6d. The trend is again the same with that of overpotentials,  $\text{IrO}_2/\text{FTO}$  the best and blank FTO the worst. Note that Fe-doping boosts the oxidation state of the Co ions of  $\text{Co}_3\text{O}_4$  by 0.3 eV as discussed earlier, giving higher oxidative powers of the Co ions for catalyzation of the OER and thus a higher TOF for  $\text{Fe-Co}_3\text{O}_4/\text{C}$  over  $\text{Co}_3\text{O}_4/\text{C}$ , 0.292 vs. 0.137  $\text{s}^{-1}$ . Modulation of the electronic structure of  $\text{Co}_3\text{O}_4$  through Fe-doping does enhance the intrinsic activity of  $\text{Co}_3\text{O}_4$ . Taking both ECSA and TOF into consideration gives the OER efficiency of the catalyst, manifested as overpotentials achieved by the catalyst at specific current densities.

### 3.3. Durability and Faradaic efficiency

In addition to electrocatalytic efficiency, catalyst durability is also essential. The durability of  $\text{Co}_3\text{O}_4/\text{C}/\text{FTO}$  and  $\text{Fe-Co}_3\text{O}_4/\text{C}/\text{FTO}$  was evaluated at the commonly used current density of 10  $\text{mA cm}^{-2}$  under a chronopotentiometric (V-t) mode and the results are given in Fig. 7a and b, respectively. The electrochemical performance of  $\text{Co}_3\text{O}_4/\text{C}/\text{FTO}$  electrode remains stable for 30 h with an increase in applied potentials of less than 10% (Fig. 7a). The applied potential needed to maintain the current density however increases rapidly after 30 h, signifying the failure of the electrode. The failure is caused mainly by the mechanical instability of the electrode, with a significant amount of catalyst detached from the FTO glass substrate as evident from the photo of the electrolyte taken at 31 h (Fig. S12, Supporting Information). As for  $\text{Fe-Co}_3\text{O}_4/\text{C}/\text{FTO}$ , its stability is much better than that of  $\text{Co}_3\text{O}_4/\text{C}/\text{FTO}$ , remaining stable for 51 h (Fig. 7b) before the mechanical failure occurring during the 52th hour (Fig. S12, Supporting Information). The improvement in electrode stability realized with Fe-doping may be attributed to the better substrate/catalyst adhesion of  $\text{Fe-Co}_3\text{O}_4/\text{C}/\text{FTO}$  because of the smaller primary particle size of  $\text{Fe-Co}_3\text{O}_4$ . Evidently, Fe-doping improves not only the catalytic efficiency, but also the stability of the electrode. As a comparison, the stability of  $\text{Fe-Co}_3\text{O}_4/\text{C}/\text{FTO}$  tested at 10  $\text{mA cm}^{-2}$  (2.5% increase in overpotential at 20 h, 6.1% at 50 h) is even better than noble metal based OER electrocatalysts, such as S-doped M-SrIrO<sub>3</sub> (~4% at 20 h) [55] and  $\text{RuO}_2/(\text{Co,Mn})_3\text{O}_4$  (8.7% at 24 h) [56], under chronopotentiometric mode in 0.5 M  $\text{H}_2\text{SO}_4$ .

The morphology and oxidation states of the catalyst was further investigated after the stability test. For morphology, SEM images of  $\text{Co}_3\text{O}_4/\text{C}/\text{FTO}$  (Fig. S13, Supporting Information) and  $\text{Fe-Co}_3\text{O}_4/\text{C}/\text{FTO}$  (Fig. S14, Supporting Information) after the stability test show that the catalysts maintain well their morphologies. Figs. S15 and S16 (Supporting Information) display the full survey XPS spectra and HR-XPS spectra of Co2p of  $\text{Co}_3\text{O}_4/\text{C}/\text{FTO}$  and  $\text{Fe-Co}_3\text{O}_4/\text{C}/\text{FTO}$ , respectively. The XPS spectra recorded after the stability test remain similar to those before the stability test, implying well maintained electronic structure of the catalyst after the stability test. The Faradaic efficiency of the acidic OER process was further tested to see if the current densities generated are contributed by the OER instead of side reactions. The oxygen generated during the acidic OER process with the working electrode,  $\text{Fe-Co}_3\text{O}_4/\text{C}/\text{FTO}$ , operating at a current density of 10  $\text{mA cm}^{-2}$  for 4 h, was compared with theoretical oxygen gas production based on the current densities recorded. The purity of the experimentally generated oxygen gas was confirmed with gas chromatography measurements to be > 99% (Fig. S17, Supporting Information). Fig. 7c shows that the amount of experimentally produced oxygen is close to that of the theoretical value, suggesting nearly 100% Faradaic efficiency of the OER and negligible contributions from other reactions.

### 3.4. Comparison of OER electrocatalytic performance with literature and OER mechanism

The electrocatalytic performances of  $\text{Fe-Co}_3\text{O}_4/\text{C}/\text{FTO}$  are compared with those of recently reported non-noble metal based OER electrocatalysts in terms of overpotentials, stability, and Faradaic efficiency (Table S2, Supporting Information). Taking all three performance indicators into consideration,  $\text{Fe-Co}_3\text{O}_4/\text{C}/\text{FTO}$  appears as one of the top non-noble metal based electrodes toward the acidic OER. It is to be noted that Faradaic efficiency of many catalysts, especially those supported on carbon-based substrates, was not reported, possibly because of the instability of the substrate itself during the acidic OER process. The enhanced OER performances are mainly attributed to the carbon coating and Fe doping of  $\text{Co}_3\text{O}_4$ , as well as the porous secondary particle structure derived from Co-MOF. For the OER, it most likely proceeds with the well accepted adsorbates evolution mechanism through partial formation of active cobalt oxyhydroxide intermediates. [57] Firstly, adsorption of water molecules onto the surface of oxygen-coordinated

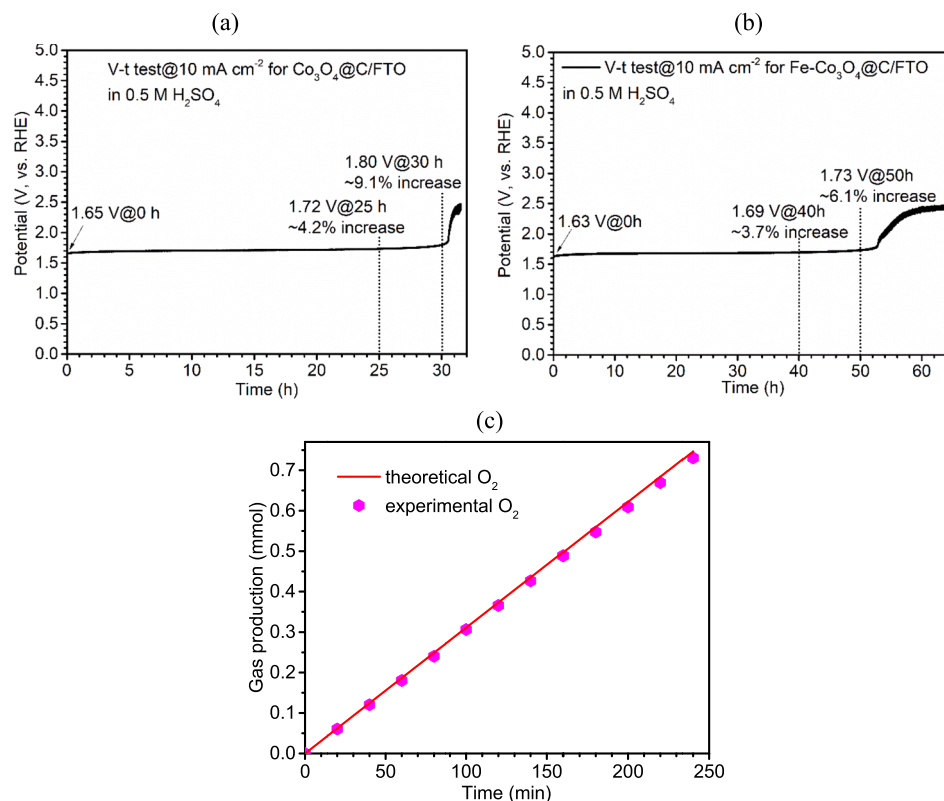


**Fig. 7.** (a) Chronopotentiometric (V-t) test for (a) Co<sub>3</sub>O<sub>4</sub>/C/FTO and (b) Fe-Co<sub>3</sub>O<sub>4</sub>/C/FTO at 10 mA cm<sup>-2</sup>. (c) Experimental and theoretical amounts of oxygen production by Fe-Co<sub>3</sub>O<sub>4</sub>/C/FTO for OER at 10 mA cm<sup>-2</sup>.

cobalt sites occurs to form the intermediate Co\*OH species (Co<sup>+</sup>), accompanied by the release of a proton and an electron. Further oxidation of Co\*OH results in formation of Co\*O species (Co<sup>2+</sup>) with further release of a proton and an electron. The oxidation proceeds further to form the active intermediate species, Co\*OOH, (Co<sup>3+</sup>) via further releasing an electron and a proton. Finally, oxygen is produced through oxidation of Co\*OOH in a one electron transfer process, with recovery of the Co active site.[57] Furthermore, it has been reported, based on density functional theory (DFT) calculations, that the adsorption energy difference between the O\* and OH\* intermediates at the active site is a dominant parameter on the overall OER activity.[24] When doping Fe into the lattice of Co<sub>3</sub>O<sub>4</sub>, DFT calculations show that the adsorption energy difference between OH\* and O\* intermediates is significantly reduced, giving enhanced OER performances [24].

#### 4. Conclusion

In summary, a simple method was developed to significantly enhance the electrochemical performances of spinel Co<sub>3</sub>O<sub>4</sub> toward catalyzation of acidic OER, through in-situ construction of a binder-free, self-standing carbon coated and Fe-doped Co<sub>3</sub>O<sub>4</sub> from a Co-MOF on FTO. The Fe-doping greatly enhanced the electrocatalytic electrochemical performances of carbon coated Co<sub>3</sub>O<sub>4</sub> for acidic OER, through reduced primary particle size and favorably modulated electronic structure of Co<sub>3</sub>O<sub>4</sub>/C induced by the Fe-doping. The Fe-Co<sub>3</sub>O<sub>4</sub>/C/FTO electrode exhibited excellent catalytic efficiency toward acidic OER with an overpotential of 396 mV at 10 mA cm<sup>-2</sup> and maintained the current density of 10 mA cm<sup>-2</sup> for more than 50 h in a highly corrosive acidic medium (0.5 M H<sub>2</sub>SO<sub>4</sub>). The electrocatalytic system (Fe-Co<sub>3</sub>O<sub>4</sub>/C/FTO) developed in this study shows great potential as non-noble metal-based anode materials that can be integrated to PEM-based water electrolyzers. Evidently, modulating the electronic structures of non-noble metal based catalysts through hetero-atom doping is a promising

approach to develop advanced non-noble metal based electrocatalysts for acidic OER. Multiple doping may take the advantages of synergistic effects to further improve the catalytic performance of the catalyst. Furthermore, introduction of ultrathin coating of conducting and acid-tolerant materials may pave the way for practical industrial applications.

#### CRediT authorship contribution statement

**Duraisamy Senthil Raja:** conceptualization, data curation, formal analysis, investigation, methodology, validation, writing - original draft, and writing - review & editing. **Po-Yin Cheng:** data curation, formal analysis, and investigation. **Chih-Chieh Cheng:** data curation, formal analysis, and investigation. **Shun-Qin Chang:** data curation and investigation. **Chun-Lung Huang:** investigation. **Shih-Yuan Lu:** conceptualization, formal analysis, funding acquisition, investigation, methodology, project administration, resources, supervision, validation, and writing - review & editing.

#### Declaration of Competing Interest

The authors declare that they have no known competing financial interests or personal relationships that could have appeared to influence the work reported in this paper.

#### Acknowledgements

The financial support offered by the Ministry of Science and Technology of Taiwan (MOST 108-2221-E-007-073-MY3 and MOST 109-2811-E-007-513) is gratefully acknowledged.



## Appendix A. Supporting information

Supplementary data associated with this article can be found in the online version at [doi:10.1016/j.apcatb.2021.120899](https://doi.org/10.1016/j.apcatb.2021.120899).

## References

- [1] X. Du, M.A. Oturan, M. Zhou, N. Belkessa, P. Su, J. Cai, C. Trellu, E. Mousset, Nanostructured electrodes for electrocatalytic advanced oxidation processes: From materials preparation to mechanisms understanding and wastewater treatment applications, *Appl. Catal. B: Environ.* 296 (2021), 120332, <https://doi.org/10.1016/j.apcatb.2021.120332>.
- [2] W. Seh Zhi, J. Kibsgaard, F. Dickens Colin, I. Chorkendorff, K. Nørskov Jens, F. Jaramillo Thomas, Combining theory and experiment in electrocatalysis: Insights into materials design, *Science* 355 (2017), eaad4998, <https://doi.org/10.1126/science.aad4998>.
- [3] B. Zhang, Y. Zheng, T. Ma, C. Yang, Y. Peng, Z. Zhou, M. Zhou, S. Li, Y. Wang, C. Cheng, Designing MOF Nanoarchitectures for Electrochemical Water Splitting, *Adv. Mater.* 33 (2021), 2006042, <https://doi.org/10.1002/adma.202006042>.
- [4] K.R.G. Lim, A.D. Handoko, S.K. Nemani, B. Wyatt, H.-Y. Jiang, J. Tang, B. Anasori, Z.W. Seh, Rational Design of Two-Dimensional Transition Metal Carbide/Nitride (MXene) Hybrids and Nanocomposites for Catalytic Energy Storage and Conversion, *ACS Nano* 14 (2020) 10834–10864, <https://doi.org/10.1021/acsnano.0c05482>.
- [5] Y. Li, Y. Sun, Y. Qin, W. Zhang, L. Wang, M. Luo, H. Yang, S. Guo, Recent Advances on Water-Splitting Electrocatalysis Mediated by Noble-Metal-Based Nanostructured Materials, *Adv. Energy Mater.* 10 (2020), 1903120, <https://doi.org/10.1002/aenm.201903120>.
- [6] J. Dong, X. Zhang, J. Huang, J. Hu, Z. Chen, Y. Lai, In-situ formation of unsaturated defect sites on converted CoNi alloy/Co-Ni LDH to activate MoS<sub>2</sub> nanosheets for pH-universal hydrogen evolution reaction, *Chem. Eng. J.* 412 (2021), 128556, <https://doi.org/10.1016/j.cej.2021.128556>.
- [7] T. Liu, P. Diao, Z. Lin, H. Wang, Sulfur and selenium doped nickel chalcogenides as efficient and stable electrocatalysts for hydrogen evolution reaction: The importance of the dopant atoms in and beneath the surface, *Nano Energy* 74 (2020), 104787, <https://doi.org/10.1016/j.nanoen.2020.104787>.
- [8] Y. Sun, K. Xu, Z. Zhao, X. Li, G. Chen, C. Li, Strongly coupled dual zerovalent nonmetal doped nickel phosphide Nanoparticles/N, B-graphene hybrid for pH-Universal hydrogen evolution catalysis, *Appl. Catal. B: Environ.* 278 (2020), 119284, <https://doi.org/10.1016/j.apcatb.2020.119284>.
- [9] Y. Zhang, C. Yang, M. Sheng, X. Yin, W. Que, J. Henzie, Y. Yamauchi, Phosphorus-doped molybdenum carbide/MXene hybrid architectures for upgraded hydrogen evolution reaction performance over a wide pH range, *Chem. Eng. J.* 423 (2021), 130183, <https://doi.org/10.1016/j.cej.2021.130183>.
- [10] A.D. Handoko, S.N. Steinmann, Z.W. Seh, Theory-guided materials design: two-dimensional MXenes in electro- and photocatalysis, *Nanoscale Horiz.* 4 (2019) 809–827, <https://doi.org/10.1039/C9NH00100J>.
- [11] X. Zou, X. Huang, A. Goswami, R. Silva, B.R. Sathe, E. Mikmeková, T. Asefa, Cobalt-Embedded Nitrogen-Rich Carbon Nanotubes Efficiently Catalyze Hydrogen Evolution Reaction at All pH Values, *Angew. Chem. Int. Ed.* 53 (2014) 4372–4376, <https://doi.org/10.1002/anie.201311111>.
- [12] X.-F. Chuah, C.-T. Hsieh, C.-L. Huang, D. Senthil Raja, H.-W. Lin, S.-Y. Lu, In-Situ Grown, Passivator-Modulated Anodization Derived Synergistically Well-Mixed Ni-Fe Oxides from Ni Foam as High-Performance Oxygen Evolution Reaction Electrocatalyst, *ACS Appl. Energy Mater.* 2 (2019) 743–753, <https://doi.org/10.1021/acsaem.8b01794>.
- [13] Z.-P. Wu, X.F. Lu, S.-Q. Zang, X.W. Lou, Non-Noble-Metal-Based Electrocatalysts toward the Oxygen Evolution Reaction, *Adv. Funct. Mater.* 30 (2020), 1910274, <https://doi.org/10.1002/adfm.201910274>.
- [14] L. An, C. Wei, M. Lu, H. Liu, Y. Chen, G.G. Scherer, A.C. Fisher, P. Xi, Z.J. Xu, C.-H. Yan, Recent Development of Oxygen Evolution Electrocatalysts in Acidic Environment, *Adv. Mater.* 33 (2021), 2006328, <https://doi.org/10.1002/adma.202006328>.
- [15] J.S. Mondschein, J.F. Callejas, C.G. Read, J.Y.C. Chen, C.F. Holder, C.K. Badding, R.E. Schaak, Crystalline Cobalt Oxide Films for Sustained Electrocatalytic Oxygen Evolution under Strongly Acidic Conditions, *Chem. Mater.* 29 (2017) 950–957, <https://doi.org/10.1021/acs.chemmater.6b02879>.
- [16] C. Mittelsteadt, T. Norman, M. Rich, J. Willey, Chapter 11 - PEM Electrolyzers and PEM Regenerative Fuel Cells Industrial View, in: P.T. Moseley, J. Garche (Eds.), *Electrochemical Energy Storage for Renewable Sources and Grid Balancing*, Elsevier, Amsterdam, 2015, pp. 159–181, <https://doi.org/10.1016/B978-0-444-62616-5.00011-5>.
- [17] Z. Chen, X. Duan, W. Wei, S. Wang, B.-J. Ni, Electrocatalysts for acidic oxygen evolution reaction: Achievements and perspectives, *Nano Energy* 78 (2020), 105392, <https://doi.org/10.1016/j.nanoen.2020.105392>.
- [18] A. Saad, D. Liu, Y. Wu, Z. Song, Y. Li, T. Najam, K. Zong, P. Tsiakaras, X. Cai, Ag nanoparticles modified crumpled borophene supported Co<sub>3</sub>O<sub>4</sub> catalyst showing superior oxygen evolution reaction (OER) performance, *Appl. Catal. B: Environ.* 298 (2021), 120529, <https://doi.org/10.1016/j.apcatb.2021.120529>.
- [19] B. Tang, J. Yang, Z. Kou, L. Xu, H.L. Seng, Y. Xie, A.D. Handoko, X. Liu, Z.W. Seh, H. Kawai, H. Gong, W. Yang, Surface-engineered cobalt oxide nanowires as multifunctional electrocatalysts for efficient Zn-Air batteries-driven overall water splitting, *Energy Storage Mater.* 23 (2019) 1–7, <https://doi.org/10.1016/j.ensm.2019.05.046>.
- [20] G.A. Kozhina, A.N. Ermakov, V.B. Fetisov, A.V. Fetisov, K.Y. Shunyaev, Electrochemical dissolution of Co<sub>3</sub>O<sub>4</sub> in acidic solutions, *Russ. J. Electrochem.* 45 (2009) 1170–1175, <https://doi.org/10.1134/S1023193509100097>.
- [21] L.M. Da Silva, J.F.C. Boodts, L.A. De Faria, Oxygen evolution at RuO<sub>2</sub>(x)+Co<sub>3</sub>O<sub>4</sub>(1-x) electrodes from acid solution, *Electrochim. Acta* 46 (2001) 1369–1375, [https://doi.org/10.1016/S0013-4686\(00\)00716-7](https://doi.org/10.1016/S0013-4686(00)00716-7).
- [22] X. Yang, H. Li, A.-Y. Lu, S. Min, Z. Idriss, M.N. Hedhili, K.-W. Huang, H. Idriss, L.-J. Li, Highly acid-durable carbon coated Co<sub>3</sub>O<sub>4</sub> nanoarrays as efficient oxygen evolution electrocatalysts, *Nano Energy* 25 (2016) 42–50, <https://doi.org/10.1016/j.nanoen.2016.04.035>.
- [23] X.-Z. Liu, T. Tang, W.-J. Jiang, Q.-H. Zhang, L. Gu, J.-S. Hu, Fe-doped Co<sub>3</sub>O<sub>4</sub> polycrystalline nanosheets as a binder-free bifunctional cathode for robust and efficient zinc-air batteries, *Chem. Commun.* 56 (2020) 5374–5377, <https://doi.org/10.1039/D0CC01024C>.
- [24] S.L. Zhang, B.Y. Guan, X.F. Lu, S. Xi, Y. Du, X.W. Lou, Metal Atom-Doped Co<sub>3</sub>O<sub>4</sub> Hierarchical Nanoplates for Electrocatalytic Oxygen Evolution, *Adv. Mater.* 32 (2020), 2002235, <https://doi.org/10.1002/adma.202002235>.
- [25] Z. Liang, T. Qiu, S. Gao, R. Zhong, R. Zou, Multi-Scale Design of Metal–Organic Framework-Derived Materials for Energy Electrocatalysis, *Adv. Energy Mater.* 43 (2021), 2003410, <https://doi.org/10.1002/aenm.202003410>.
- [26] X.F. Lu, Y. Fang, D. Luan, X.W.D. Lou, Metal–Organic Frameworks Derived Functional Materials for Electrochemical Energy Storage and Conversion: A Mini Review, *Nano Lett.* 21 (2021) 1555–1565, <https://doi.org/10.1021/acs.nanolett.0c04898>.
- [27] Z. Li, M. Song, W. Zhu, W. Zhuang, X. Du, L. Tian, MOF-derived hollow heterostructures for advanced electrocatalysis, *Coord. Chem. Rev.* 439 (2021), 213946, <https://doi.org/10.1016/j.ccr.2021.213946>.
- [28] J.M. Gonçalves, P.R. Martins, D.P. Rocha, T.A. Matias, M.S.S. Julião, R.A. A. Munoz, L. Angnes, Recent trends and perspectives in electrochemical sensors based on MOF-derived materials, *J. Mater. Chem. C* 9 (2021) 8718–8745, <https://doi.org/10.1039/D1TC02025K>.
- [29] C. Chen, Y. Tuo, Q. Lu, H. Lu, S. Zhang, Y. Zhou, J. Zhang, Z. Liu, Z. Kang, X. Feng, D. Chen, Hierarchical trimetallic Co-Ni-Fe oxides derived from core-shell structured metal-organic frameworks for highly efficient oxygen evolution reaction, *Appl. Catal. B: Environ.* 287 (2021), 119953, <https://doi.org/10.1016/j.apcatb.2021.119953>.
- [30] W.-D. Zhang, H. Yu, T. Li, Q.-T. Hu, Y. Gong, D.-Y. Zhang, Y. Liu, Q.-T. Fu, H.-Y. Zhu, X. Yan, Z.-G. Gu, Hierarchical trimetallic layered double hydroxide nanosheets derived from 2D metal-organic frameworks for enhanced oxygen evolution reaction, *Appl. Catal. B: Environ.* 264 (2020), 118532, <https://doi.org/10.1016/j.apcatb.2019.118532>.
- [31] H. Zou, B. He, P. Kuang, J. Yu, K. Fan, Metal–Organic Framework-Derived Nickel–Cobalt Sulfide on Ultrathin MXene Nanosheets for Electrocatalytic Oxygen Evolution, *ACS Appl. Mater. Interfaces* 10 (2018) 22311–22319, <https://doi.org/10.1021/acsaami.8b06272>.
- [32] X. Wang, L. Chai, J. Ding, L. Zhong, Y. Du, T.-T. Li, Y. Hu, J. Qian, S. Huang, Chemical and morphological transformation of MOF-derived bimetallic phosphide for efficient oxygen evolution, *Nano Energy* 62 (2019) 745–753, <https://doi.org/10.1016/j.nanoen.2019.06.002>.
- [33] S.-H. Chae, A. Muthurasu, T. Kim, J.S. Kim, M.-S. Khil, M. Lee, H. Kim, J.Y. Lee, H. Y. Kim, Templated fabrication of perfectly aligned metal-organic framework-supported iron-doped copper-cobalt selenide nanostructure on hollow carbon nanofibers for an efficient trifunctional electrode material, *Appl. Catal. B: Environ.* 293 (2021), 120209, <https://doi.org/10.1016/j.apcatb.2021.120209>.
- [34] B.K. Kang, S.Y. Im, J. Lee, S.H. Kwag, S.B. Kwon, S. Tiruneh, M.-J. Kim, J.H. Kim, W.S. Yang, B. Lim, D.H. Yoon, In-situ formation of MOF derived mesoporous Co<sub>3</sub>N/amorphous N-doped carbon nanocubes as an efficient electrocatalytic oxygen evolution reaction, *Nano Res.* 12 (2019) 1605–1611, <https://doi.org/10.1007/s12274-019-2399-3>.
- [35] X. Li, S. You, J. Du, Y. Dai, H. Chen, Z. Cai, N. Ren, J. Zou, ZIF-67-derived Co<sub>3</sub>O<sub>4</sub>@carbon protected by oxygen-buffering CeO<sub>2</sub> as an efficient catalyst for boosting oxygen reduction/evolution reactions, *J. Mater. Chem. A* 7 (2019) 25853–25864, <https://doi.org/10.1039/C9TA08926H>.
- [36] S. Li, Y. Gao, N. Li, L. Ge, X. Bu, P. Feng, Transition metal-based bimetallic MOFs and MOF-derived catalysts for electrochemical oxygen evolution reaction, *Energy Environ. Sci.* 14 (2021) 1897–1927, <https://doi.org/10.1039/D0EE03697H>.
- [37] H. Wang, B.-H. Chen, D.-J. Liu, Metal–Organic Frameworks and Metal–Organic Gels for Oxygen Electrocatalysis: Structural and Compositional Considerations, *Adv. Mater.* 33 (2021), 2008023, <https://doi.org/10.1002/adma.202008023>.
- [38] M. Etzi Coller Pascuzzi, M. van Velzen, J.P. Hofmann, E.J.M. Hensen, On the Stability of Co<sub>3</sub>O<sub>4</sub> Oxygen Evolution Electrocatalysts in Acid, *ChemCatChem* 13 (2021) 459–467, <https://doi.org/10.1002/cctc.202001428>.
- [39] J.D. Benck, B.A. Pinaud, Y. Gorlin, T.F. Jaramillo, Substrate Selection for Fundamental Studies of Electrocatalysts and Photoelectrodes: Inert Potential Windows in Acidic, Neutral, and Basic Electrolyte, *PLOS ONE* 9 (2014), e107942, <https://doi.org/10.1371/journal.pone.0107942>.
- [40] N.K. Chaudhari, H. Jin, B. Kim, K. Lee, Nanostructured materials on 3D nickel foam as electrocatalysts for water splitting, *Nanoscale* 9 (2017) 12231–12247, <https://doi.org/10.1039/C7NR04187J>.
- [41] H.-W. Lin, D. Senthil Raja, X.-F. Chuah, C.-T. Hsieh, Y.-A. Chen, S.-Y. Lu, Bi-metallic MOFs possessing hierarchical synergistic effects as high performance electrocatalysts for overall water splitting at high current densities, *Appl. Catal. B: Environ.* 258 (2019), 118023, <https://doi.org/10.1016/j.apcatb.2019.118023>.
- [42] D. Senthil Raja, H.-W. Lin, S.-Y. Lu, Synergistically well-mixed MOFs grown on nickel foam as highly efficient durable bifunctional electrocatalysts for overall

- water splitting at high current densities, *Nano Energy* 57 (2019) 1–13, <https://doi.org/10.1016/j.nanoen.2018.12.018>.
- [43] D. Senthil Raja, C.-L. Huang, Y.-A. Chen, Y. Choi, S.-Y. Lu, Composition-balanced trimetallic MOFs as ultra-efficient electrocatalysts for oxygen evolution reaction at high current densities, *Appl. Catal. B: Environ.* 279 (2020), 119375, <https://doi.org/10.1016/j.apcatb.2020.119375>.
- [44] E. Detsi, J.B. Cook, B.K. Lesel, C.L. Turner, Y.-L. Liang, S. Robbenolt, S.H. Tolbert, Mesoporous Ni<sub>60</sub>Fe<sub>30</sub>Mn<sub>10</sub>-alloy based metal/metal oxide composite thick films as highly active and robust oxygen evolution catalysts, *Energy Environ. Sci.* 9 (2016) 540–549, <https://doi.org/10.1039/C5EE02509E>.
- [45] T.-Y. Liang, D. Senthil Raja, K.C. Chin, C.-L. Huang, S.A.P. Sethupathi, L.K. Leong, D.-H. Tsai, S.-Y. Lu, Bimetallic Metal–Organic Framework-Derived Hybrid Nanostructures as High-Performance Catalysts for Methane Dry Reforming, *ACS Appl. Mater. Interfaces* 12 (2020) 15183–15193, <https://doi.org/10.1021/acsami.0c00086>.
- [46] X. Zhao, B. Pattengale, D. Fan, Z. Zou, Y. Zhao, J. Du, J. Huang, C. Xu, Mixed-Node Metal–Organic Frameworks as Efficient Electrocatalysts for Oxygen Evolution Reaction, *ACS Energy Lett.* 3 (2018) 2520–2526, <https://doi.org/10.1021/acseenergylett.8b01540>.
- [47] C. Wang, H.-J. Bongard, M. Yu, F. Schüth, Highly Ordered Mesoporous Co<sub>3</sub>O<sub>4</sub> Electrocatalyst for Efficient, Selective, and Stable Oxidation of 5-Hydroxymethyl-furfural to 2,5-Furandicarboxylic Acid, *ChemSusChem* (2021), <https://doi.org/10.1002/cssc.202002762>.
- [48] A. Li, H. Ooka, N. Bonnet, T. Hayashi, Y. Sun, Q. Jiang, C. Li, H. Han, R. Nakamura, Stable Potential Windows for Long-Term Electrocatalysis by Manganese Oxides Under Acidic Conditions, *Angew. Chem. Int. Ed.* 58 (2019) 5054–5058, <https://doi.org/10.1002/anie.201813361>.
- [49] K.-L. Yan, J.-F. Qin, J.-H. Lin, B. Dong, J.-Q. Chi, Z.-Z. Liu, F.-N. Dai, Y.-M. Chai, C.-G. Liu, Probing the active sites of Co<sub>3</sub>O<sub>4</sub> for the acidic oxygen evolution reaction by modulating the Co<sup>2+</sup>/Co<sup>3+</sup> ratio, *J. Mater. Chem. A* 6 (2018) 5678–5686, <https://doi.org/10.1039/C8TA00070K>.
- [50] W.L. Kwong, C.C. Lee, A. Shchukarev, J. Messinger, Cobalt-doped hematite thin films for electrocatalytic water oxidation in highly acidic media, *Chem. Commun.* 55 (2019) 5017–5020, <https://doi.org/10.1039/C9CC01369E>.
- [51] J. Wu, M. Liu, K. Chatterjee, K.P. Hackenberg, J. Shen, X. Zou, Y. Yan, J. Gu, Y. Yang, J. Lou, P.M. Ajayan, Exfoliated 2D Transition Metal Disulfides for Enhanced Electrocatalysis of Oxygen Evolution Reaction in Acidic Medium, *Adv. Mater. Interfaces* 3 (2016), 1500669, <https://doi.org/10.1002/admi.201500669>.
- [52] J.S. Mondschein, K. Kumar, C.F. Holder, K. Seth, H. Kim, R.E. Schaak, Intermetallic Ni<sub>2</sub>Ta Electrocatalyst for the Oxygen Evolution Reaction in Highly Acidic Electrolytes, *Inorg. Chem.* 57 (2018) 6010–6015, <https://doi.org/10.1021/acs.inorgchem.8b00503>.
- [53] C.C.L. McCrory, S. Jung, J.C. Peters, T.F. Jaramillo, Benchmarking Heterogeneous Electrocatalysts for the Oxygen Evolution Reaction, *J. Am. Chem. Soc.* 135 (2013) 16977–16987, <https://doi.org/10.1021/ja407115p>.
- [54] S. Anantharaj, S.R. Ede, K. Karthick, S. Sam Sankar, K. Sangeetha, P.E. Karthik, S. Kundu, Precision and correctness in the evaluation of electrocatalytic water splitting: revisiting activity parameters with a critical assessment, *Energy Environ. Sci.* 11 (2018) 744–771, <https://doi.org/10.1039/C7EE03457A>.
- [55] M. You, L. Gui, X. Ma, Z. Wang, Y. Xu, J. Zhang, J. Sun, B. He, L. Zhao, Electronic tuning of SrIrO<sub>3</sub> perovskite nanosheets by sulfur incorporation to induce highly efficient and long-lasting oxygen evolution in acidic media, *Appl. Catal. B: Environ.* 298 (2021), 120562, <https://doi.org/10.1016/j.apcatb.2021.120562>.
- [56] S. Niu, X.-P. Kong, S. Li, Y. Zhang, J. Wu, W. Zhao, P. Xu, Low Ru loading RuO<sub>2</sub>/(Co,Mn)<sub>3</sub>O<sub>4</sub> nanocomposite with modulated electronic structure for efficient oxygen evolution reaction in acid, *Appl. Catal. B: Environ.* 297 (2021), 120442, <https://doi.org/10.1016/j.apcatb.2021.120442>.
- [57] Z. Shi, X. Wang, J. Ge, C. Liu, W. Xing, Fundamental understanding of the acidic oxygen evolution reaction: mechanism study and state-of-the-art catalysts, *Nanoscale* 12 (2020) 13249–13275, <https://doi.org/10.1039/D0NR02410D>.